Section 2

Data sets, diagnostic and dynamical investigations, statistical post-processing, reanalysis, and associated studies.

Cyclone/anticyclone activity over the Caspian Sea basin

M.G. Akperov[1], I.I. Mokhov[1], U. Tagiyeva[2], M.A. Dembitskaya[1]

[1] A.M. Obukhov Institute of Atmospheric Physics, RAS, Moscow, Russia
[2] Institute of Geography of Azerbaijan National Academy of Sciences, Baku, Azerbaijan

Variations of the hydrological cycle in the Caspian Sea basin, including precipitation over the Volga River basin and the Caspian Sea level (CSL), are among the strongest regional variations during the last century (Arpe et al., 1999; Arpe et al., 2000). They are related to variations of cyclonic activity in the basin (Mokhov et al., 1995; Mokhov and Semenov, 1997). In particular, the statistically significant tendency of increase of cyclonic activity over the Caspian Sea basin during 1980s is related with a strong increase of CSL.

We analyzed seasonal cyclone and anticyclone activity over the Caspian Sea basin (40-60^{o} E) for the periods of the CSL rise (1979-1995 - II) and drop (1950-1978 – I and 1996-2016 - III). Cyclone and anticyclone characteristics were calculated from 6-hourly mean data for sea level pressure from NCEP/NCAR reanalysis. Figure 1 shows the latitudinal distribution of cyclone and anticyclone frequency (per season) in winter and summer for the different periods.

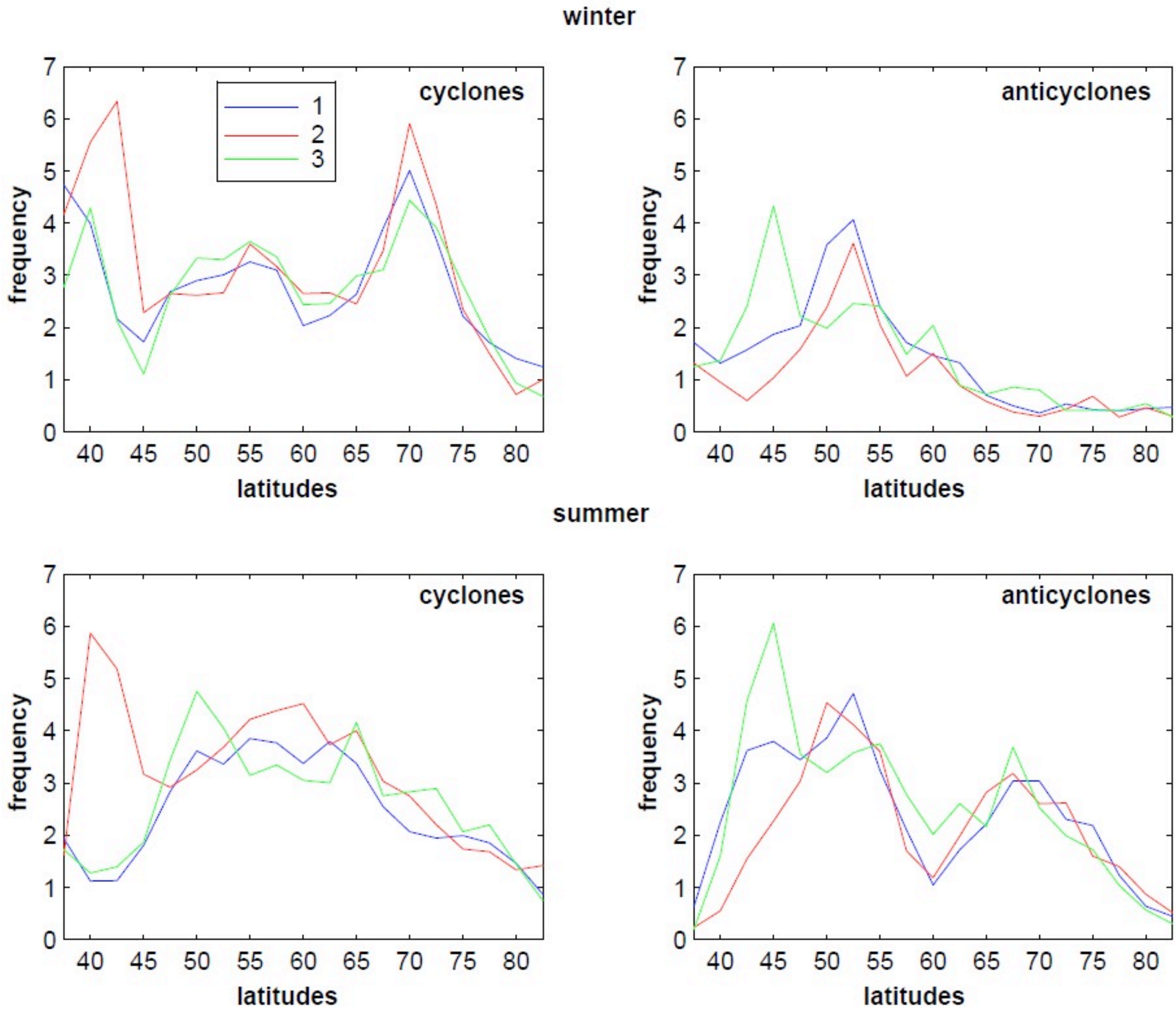

Fig. 1. Latitudinal distribution of cyclone and anticyclone frequency (per season) in winter and summer for different periods: 1 – 1950-1978, 2 – 1979-1995, 3 – 1996-2016.

Meridional distributions of cyclone/anticyclone frequency on Fig. 1 are very different in winter and in summer. Frequency of cyclones in winter shows two remarkable maxima near 70^{o}N and near 40^{o}N while in summer cyclone frequency is decreasing from middle latitudes to high and low latitudes (except period II). Frequency of anticyclones shows maximum values between 45^{o}N and 58^{o}N in both seasons with higher frequencies in summer. Anticyclone frequency has an additional maximum in summer in high latitudes (near 67^{o}N).

The strongest variations in cyclone/anticyclone frequency are noted in the Caspian Sea region (between 37-47^{o} N) in both seasons. The cyclone frequency is higher in this region during the period of the CSL rise and lower for the periods of the CSL drop with the opposite sign variations for frequency of anticyclones. The most significant variations are noted in summer.

This work was supported by the RFBR and RAS.

References

Arpe K., L. Bengtsson, G.S. Golitsyn, I.I. Mokhov, V.A. Semenov and S.P. Sporyshev, 1999: Analysis and modelling of hydrological cycle changes in the Caspian Sea basin. *Doklady Earth Sci.,* **366**, 248-252.

Arpe K., L. Bengtsson, G.S. Golitsyn, I.I. Mokhov, V.A. Semenov and S.P. Sporyshev, 2000: Connection between Caspian Sea level variability and ENSO. *Geophys. Res. Lett.,* **27**, 2693-2699.

Mokhov I.I., V.K. Petukhov and A.O. Senatorsky, 1995: Sensitivity of storm track activity and blockings to global climatic changes: Diagnostics and modelling. *Publ. Acad. Finland,* **6/95**, 438-441.

Mokhov I.I. and V.A. Semenov, 1997: Cyclonic activity and hydrological cycle over Caspian Sea region. *Research Activities in Atmospheric and Oceanic Modelling* (ed. A. Staniforth), CAS/JSC WGNE, WMO/TD-No. 792, 2.35-2.36.

INFLUENCE OF ATMOSPHERIC HEAT TRANSPORT ON AMPLIFICATION OF WINTER WARMING IN THE ARCTIC

Genrikh Alekseev[1)], Svetlana Kuzmina[2)], Aleksandra Urazgildeeva[3)] and Leonid Bobylev[2)]
[1] Arctic and Antarctic Research Institute (alexgv@aari.ru), [2] Nansen Centre, [3] St. Petersburg State University St. Petersburg, Russian Federation

Assessments of the energy budget show that the main part of incoming energy into the Arctic in winter enters with meridional atmospheric heat transport (MAHT) (Nakamura, Oort, 1988). However, global climate model simulations and calculations from reanalysis data indicate that MAHT has lesser importance than local feedbacks for explaining the Arctic amplification (Hwang et al., 2011). The objective of our investigation is to establish the link between the amplified winter warming in the high Arctic and the MAHT across 70 ° N.

Data from ERA/Interim (Dee et al., 2011) for 1979-2014 were used. The data included monthly air temperature, water vapor content, meridional component of the wind at grid points 1°×1° from 1000 to 100 hPa spaced-apart 50 hPa. The total values of meridional transport of heat and moisture through a unit vertical from the surface to 10 hPa and integral from the surface to 10 hPa water vapor content in each grid point were also used. The calculations of MAHT into 70°-90°N area based on the formulas presented in (Nakamura, Oort, 1988).

The total meridional atmospheric transport of sensible heat across the 70°N "wall" calculated from vertically integrated MAHT values in every grid point in ERA/Interim area is uncorrelated with mean air temperature in 70-90^{0}N area in every month. The total MAHT of latent heat correlates with the air temperature in winter months only. To understand the lack of correlation we construct the spatial distribution of anomalies of monthly mean air temperature and water vapor content at isobaric surfaces averaged for 1979-2014, which show two regions with maximal anomalies. These regions corresponded to the parts of the 70^{0}N circle across which the heat and moisture enter the 70-90^{0}N area. We referred to these parts as Atlantic (0-80^{0}E) and Pacific (200-230°E) "gates" [Alekseev et al., 2016]. Further, we estimated and analyzed MAHT across these "gates" for sensible (J_T) and latent (J_Q) heat fluxes across unit normal area at every isobaric surface as

$(JT)_{pgk} = (C_p\rho\langle TV\rangle)_{pgk}$ and $(JQ)_{pgk} = (L\rho\langle QV\rangle)_{pgk}$,

where $C_p = 1005$ J(kgK)$^{-1}$; $L = 2.50\times10^6$Jkg^{-1}; ρ is the air density, kgm^{-3}; Q is the water vapor content (kgkg^{-1}); V is the meridional wind, mc^{-1}; p denotes the isobaric surface, g is for year, m is month, and k = 1 or 2 for 0-80°E and 200-230°E, respectively.

Figure 1 shows the vertical profiles of V, JT , and JQ averaged along 70^0 N (blue), the Atlantic region (red), and the Pacific region (green). Winter MAHTs across 70°N into the Arctic take place up to 750 hPa and mainly through the Atlantic "gate". They show a positive transport's trend, 5-7 years cyclicity (Fig.2) and correlate with mean surface air temperature (SAT) in the 70-90°N area (Fig.3). MAHTs across the Atlantic "gate" influence the winter SAT at most part of the 70-90°N area with maximum at the Barents and Kara Seas (Fig. 4,a). The same correlation pattern results from ECHAM model control experiment data in CMIP5 (Fig.4,b) (Taylor et.al, 2012).

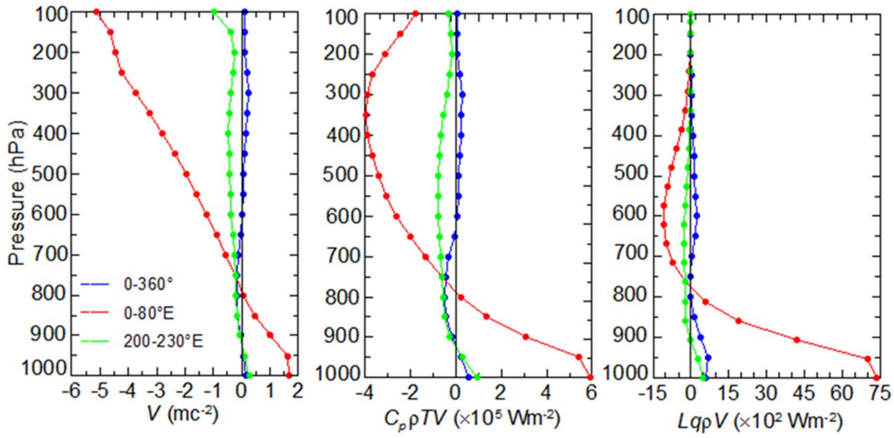

Figure 1. Vertical profiles of the meridional velocity wind component (a); the transport of sensible (b) and latent (c) heat averaged along 70N (blue), the Atlantic region (red), and the Pacific region (green).

p

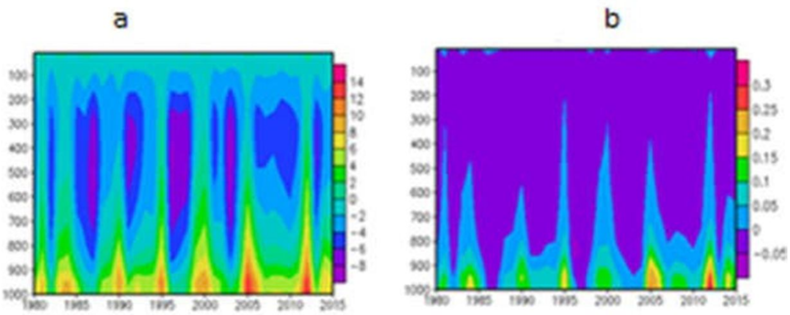

Figure 2. Winter MAHT of sensible (a, 10^5 Wm^{-2}) and latent (b, 10^5 Wm^{-2}) heat across the Atlantic "gate".

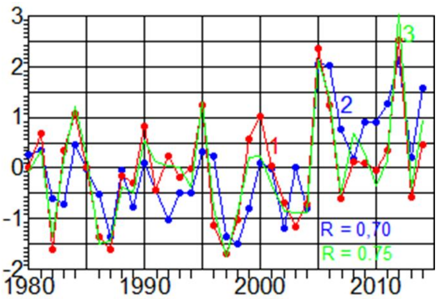

Figure 3. Standardized values of winter SAT in 70-90^{0}N (1), MAHT of sensible (2) and latent (3) heat across Atlantic "gate" at 1000 hPa surface. R are correlation coefficients between SAT and MAHTs.

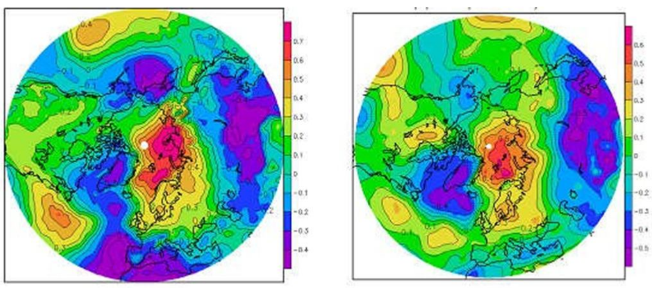

Figure 4. Pattern of correlation coefficients between winter sensible MAHT through Atlantic "gate" at 1000 hPa and winter SAT calculated on base of ERA-Interim 1980-2015 data (a) and control experiment data of ECHAM model from CMIP5.

This study is supported by RFBR grant 15-05-03512.

References

Alekseev G.V., S. I. Kuzmina, A. V. Urazgildeeva, L. P. Bobylev. Impact of atmospheric heat and moisture transport on Arctic warming in winter. Fundamental and applied climatology. 2016, vol. 1, p. 43–63 (in Russian).

Dee,D. P., and 35 co-authors. 2011. The ERA-Interim reanalysis: Configuration and performance of the data assimilation system. - Quart. J. R. Meteorol. Soc., vol. 137, № 656, 553-597 p.

Hwang, Y.-T., Frierson D. M. W., Kay J. E. 2011. Coupling between Arctic feedbacks and changes in poleward energy transport. – Geophys. Res. Lett., vol. 38.

Nakamura, N., and A. H. Oort (1988), Atmospheric heat budgets of the polar regions, J. Geophys. Res., 93(D8), 9510 – 9524.

Taylor, K.E., R.J. Stouffer, G.A. Meehl: An Overview of CMIP5 and the experiment design." Bull. Amer. Meteor. Soc., **93**, 485-498, 2012.

INFLUENCE OF SST ANOMALIES IN LOW LATITUDES ON ATMOSPHERIC HEAT TRANSPORT TO THE ARCTIC

G. Alekseev[1], S. Kuzmina[2], N. Glok[1]

[1] Arctic and Antarctic Research Institute, St. Petersburg, Russian Federation (alexgv@aari.ru)

[2] Nansen Centre, St. Petersburg, Russian Federation (Svetlana.Kuzmina@niersc.spb.ru)

The purpose of the study is to assess the influence of anomalies of the ocean surface temperature (SST) in the low latitudes of the Atlantic, Indian and Pacific oceans on the change in the winter meridional atmospheric heat transport to the Arctic and to propose the process-based explanation of this influence. Estimates of meridional atmospheric heat transport (MAHT) to the Arctic through the Atlantic "gate" (0 – 80° E at 70 ° N) in winter (December-February) 1980- 2015 fulfilled on the basis of ERA-Interim show [1] the main contribution of MAHT to the anomaly of winter surface air temperature (SAT) in the Arctic. Inter-annual variability of winter MAHT includes a trend and 5-7 years cyclicity, originated presumably from SST anomalies in the low latitudes of the Atlantic, Indian and Pacific oceans. To inspect this assumption, the area and month with maximal correlation between SST and winter MAHT, as well as the respective lag were found for each ocean [2]. Fig.1 shows the correlation between SST anomaly in October and winter MAHT with a 27-month lag. Fig.2 presents time series of SST for red areas in Fig.1 and winter MAHT to the Arctic for 1982-2014.

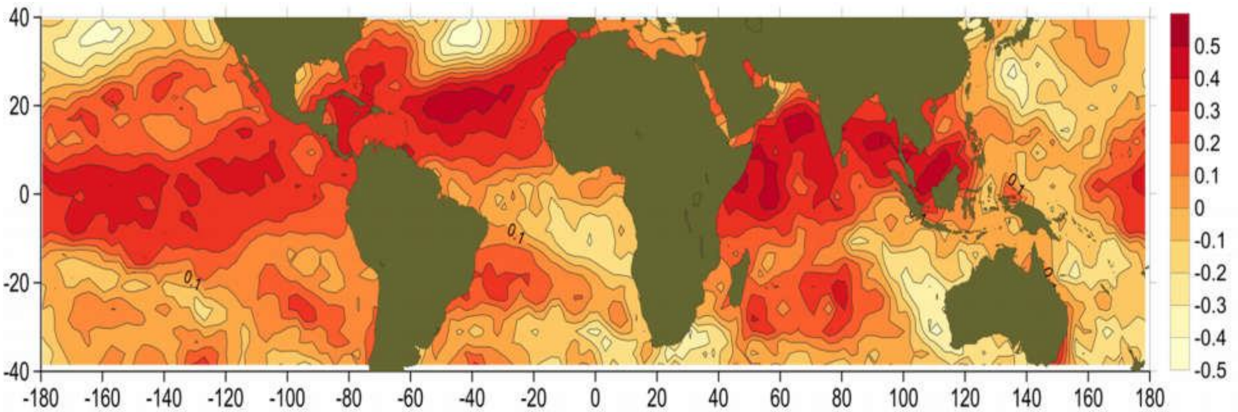

Figure 1. Correlation coefficients between SST anomalies in October in low latitude areas of the Pacific, Atlantic and Indian and anomalies of winter MAHT with a 27-month lag.

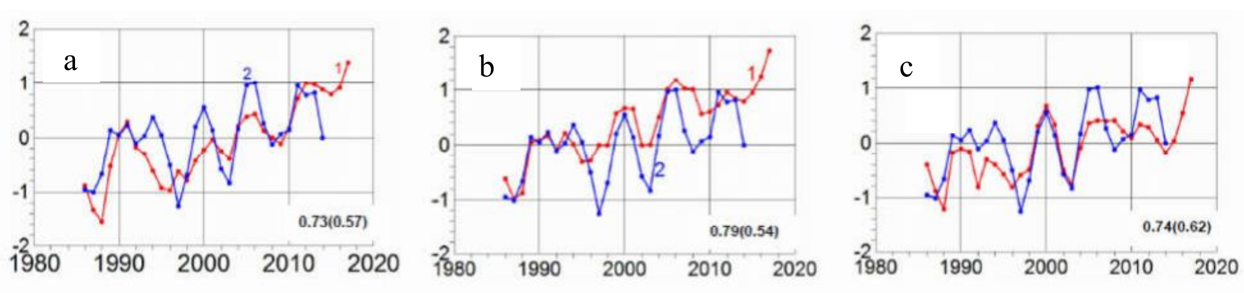

Figure 2. Time series of normalized SST (1) and MAHT (2) anomalies smoothed with a 3- year window. a – SST in the Indian Ocean in October and winter MAHT 27 months later; b – SST in the Atlantic, Indian, Pacific Oceans in October and winter MAHT after 27 months; c – SST in 10°N - 10°S area in August and winter MAHT after 30 months. Numbers in the bottom right corners are the correlation coefficients between (1) and (2). The values in the brackets are for the detrended time series.

The SST anomalies influence the atmospheric circulation through the NAO mode that is correlated significantly and negatively with SST (Fig. 3). The SST influence on the oceanic heat transport to the Arctic is confirmed by the correlation between SST anomalies in low latitudes and water temperature in 50-200m layer at section along the Kola meridian in the Barents Sea (table 1).

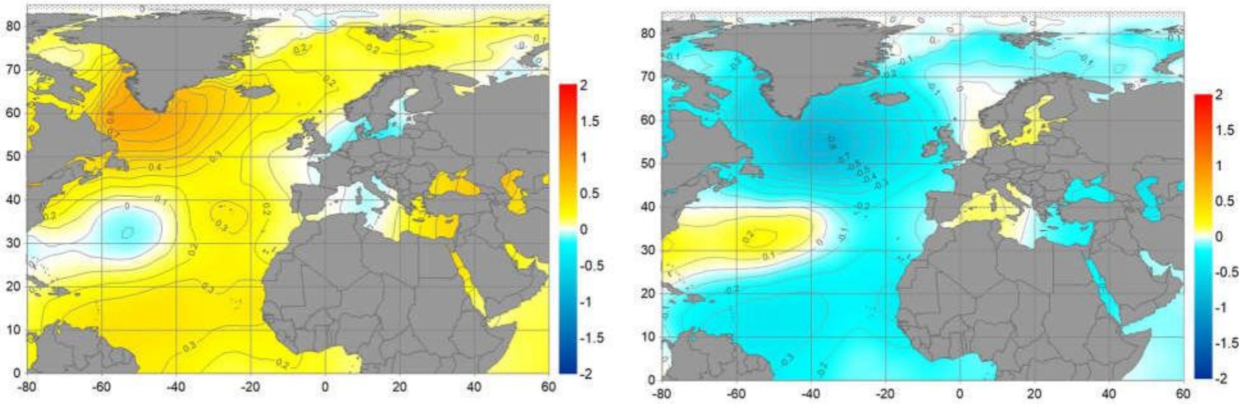

Figure 3. Composites of annual SST anomalies under strong negative (a) and positive (b) annual NAO.

Table 1. Correlation between SST anomalies in low latitudes and mean water temperature in 50- 200 m layer at section along the Kola meridian [http://www/pinro.ru/ /labs/labhidro/]. Slash divides coefficients for the raw and detrended series.

SST anomalies	Corr. coefficients (lag, months)
In Atlantic Ocean , October	0.76/0.46 (27)
In Indian Ocean, October	0.74/0.49 (27)
In Pacific Ocean, July	0.15/0.11 (30)
In area 10°N - 10°S, August	0.55/0.34 (29)

Conclusions

The effect of SST anomalies in the low latitudes of the Atlantic, Indian and Pacific Oceans on the winter atmospheric heat transport to the Arctic through the "Atlantic gates" at 70^{0}N (0 to 80°E) and on the inflow of water from the North Atlantic into the Barents Sea has been established.

The delay (> 2 years) of the reaction of atmospheric and oceanic heat influxes to the Arctic on SST anomaly means that the influence is realized by the interaction of oceanic and atmospheric circulation modes.

It is the North Atlantic Oscillation (NAO) in the atmosphere, which is negatively correlated with the anomalies of low-latitude SSTs in all three oceans.

Negative NAO mode prevails with a positive SST anomaly at low latitudes and corresponds to positive SST anomaly in the high latitudes of the North Atlantic, which manifests themself three years later in the Norwegian and Barents Seas.

The oceanic circulation system, including the Gulf Stream, the North Atlantic Current and its continuation in the Nordic Seas spreads the influence of the SST anomaly to the Arctic. As a result, after 2.25 years the temperature of the water in the Barents Sea increases and the winter atmospheric heat transport to the Arctic intensifies.

The work is supported by RFBR grant 15-05-03512.

References

1. G. V. Alekseev, S. I. Kuzmina, A. V. Urazgildeeva, L. P. Bobylev. Impact of atmospheric heat and moisture transport on Arctic warming in winter. Fundamental and Applied Climatology. 2016, v1, p 43–63 (in Russian).

2. G. V. Alekseev, S. I. Kuzmina, N.Glok. Influence of water temperature anomalies in the low latitudes of the ocean on the atmospheric transport of heat to the Arctic. Fundamental and Applied Climatology. 2017, №1, p. 106-123 (in Russian).

INFLUENCE OF THE EQUATORIAL NORTH ATLANTIC ON THE SEA ICE SHRINKING IN THE ARCTIC

G. Alekseev and N. Glok

Arctic and Antarctic Research Institute, St. Petersburg, Russian Federation (alexgv@aari.ru)

The sea surface temperature (SST) anomalies in low latitudes affect the climate change because of the large amount of heat accumulated in this part of the World Ocean [Palmer et al., 2007]. In this region, up to the end of summer (September-October) SST reaches the highest values and greatly affects the Arctic climate. Presumably, the mechanism of the influence of the SST anomalies on the Arctic includes the interaction of the atmospheric and oceanic circulation patterns, such as NAO, Hadley and Ferrel cells for the atmosphere, and the ocean Gulf Stream, the North Atlantic and the Norwegian currents. To investigate the relationship between the circulation patterns, the data of monthly SST from HadISST dataset for 1951-2013 (http://www.metoffice.gov.uk/) were used. Also involved were the data on the water temperature at Kola section in the Barents Sea for 1951-2013 (http://www/pinro.ru/n22/labs/labhidro), monthly sea ice extent (SIE) data in the Arctic (http://www.aari.ru/datasets) and NAO index data (http://www.cpc.ncep.noaa.gov/). Multivariate correlation analysis was used to determine the maximum correlation coefficients between the SST anomalies and the climate characteristics and the corresponding delays. The location of the area of SST anomalies in the North Atlantic, which is influenced by the Arctic SIE is found (fig.1 a). This area is the same for SIE in all months, but with different delays for every monthly SIE [Alekseev et al., 2016]. Fig. 1 b presents the time series of October SST anomalies and SIE 38 months later in December. The positive SST anomalies intensify and extend Hadley and Ferrel cells in the atmosphere [Adam et al., 2014; Huang and McElroy, 2014]. As a result, the meridional atmospheric circulation is enhanced. The oceanic heat transport by Gulfstream, North Atlantic/ Western Shpitsbergen and Norwegian currents also increases (fig. 2). The NAO circulation is diminished under positive SST anomalies (fig.3). Under negative NAO phase, zonal winds in the atmosphere over the Atlantic north of 40 ° N are followed by the decreased heat flux from the ocean. Thus, the NAO participates in the transmission of the influence of low-latitude SST anomalies through the impact on the SST north of 40 ° N. Finally, the strengthening of the oceanic heat inflow to the Norwegian and Barents seas and the decrease of winter spread of sea ice cover in the Arctic occurred.

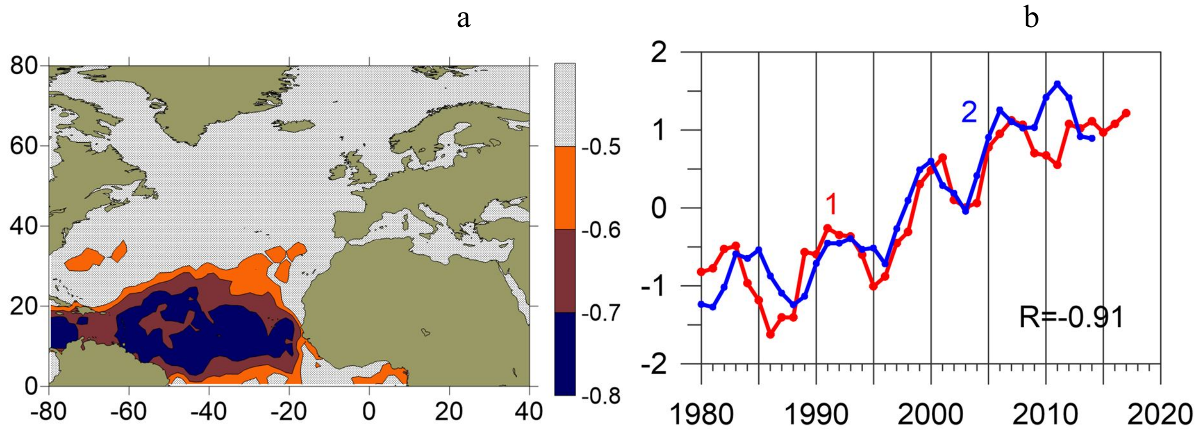

Figure 1. a) pattern of correlation coefficients between SST anomalies in October and December SIE in the Arctic after 38 months, b) standardized anomalies of October SST (1) and December SIE (2) both smoothed by 3-year averaging. R is the correlation coefficient between (1) and (2). The correlation between detrended series is -0.78. Note that the sign for the both series reversed.

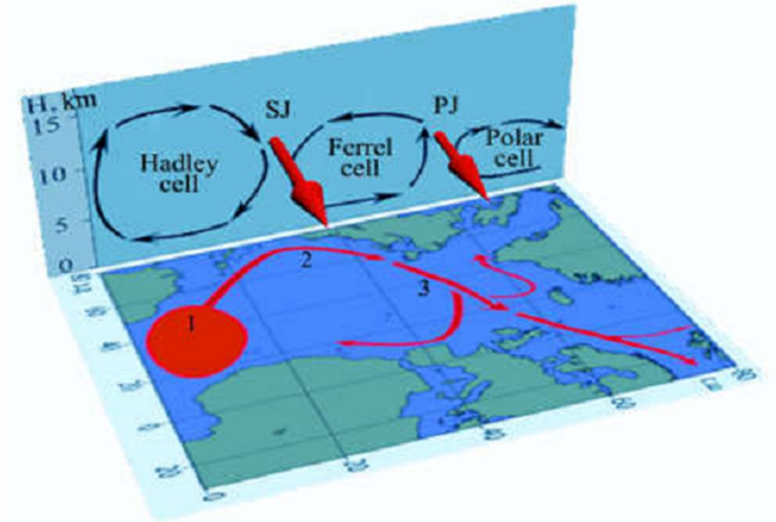

Figure 2. Idealized depiction of the SST anomaly effect on the Arctic. 1 – SST anomaly, 2 – Gulfstream, 3 – North Atlantic, Norwegian and West Spitsbergen currents, SJ – Subtropical jet, PJ – polar jet.

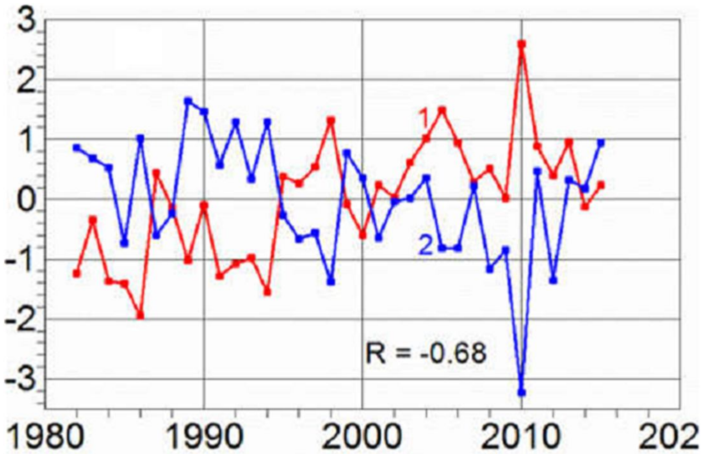

Figure 3. Normalized anomalies of annual SST (1) and annual NAO index (2). R is the correlation coefficient.

Conclusions

The relationship between the SST anomalies in low latitudes of the North Atlantic and the SIE anomalies in the Arctic with a lag of up to 3 years is established. The mechanism of remote influence of SST anomalies to the Arctic includes interaction between atmospheric and oceanic circulation modes that drive the heat transport to high latitudes.

References

Alekseev G.V., Glok N.I. Influence of equatorial North Atlantic on warming and sea iceshrinking in the Arctic. Problemi Arctiki i Antarctiki, 2016, №4 (110), 80-87. (In Russian).

Adam O., Schneider T., Harnik N. 2014. Role of Changes in Mean Temperatures versus Temperature Gradients in the Recent Widening of the Hadley Circulation. J. Clim., vol. 27, No.19, p. 7450–7461.

Huang J., McElroy M.B. 2014. Contributions of the Hadley and Ferrel Circulations to the Energetics of the Atmosphere over the Past 32 Years. J. Climate, vol. 27, p. 2656–2666.

Palmer M.D., Haines K., Tett S.F.B., Ansell T.J. 2007. Isolating the signal of ocean globalwarming. Geophys. Res. Lett., vol. 34, L23610; doi: 10.1029/2007GL031712.

Cloudiness and sea ice mutual variations in the Antarctic: dependence on Antarctic oscillation

Chernokulsky A.V., Mokhov I.I.
A.M. Obukhov Institute of Atmospheric Physics RAS, Moscow, Russia
e-mail: a.chernokulsky@ifaran.ru

Cloudiness and sea ice both act in polar amplification feedbacks. Moreover, changes of cloudiness characteristics and sea-ice extent in the polar regions are closely tied. Cloudiness changes may depend on sea ice variability and vice versa. In particular, in the Atlantic part of the Arctic, cloudiness and sea-ice show statistically significant negative correlation with each other for the last 80 years with the correlation coefficient –0.38 (Chernokulsky et al., 2017).

Variations of clouds and sea ice display significant differences in the Antarctic and Arctic. The largest changes (trends and variability) of total cloud fraction (TCF) from satellite observations (PATMOS-x and CM SAF satellite data) were noted during last decades in summer in both Hemispheres (July-August-September in the Arctic and January-February-March in the Antarctic). Sea-ice extent (SIE) decreased in the Arctic and increased in the Antarctic during the last four decades in all seasons (according to NSIDC data). For the Arctic (mean for the region 70N-90N), negative SIE-TCF correlation coefficient (R) was noted from satellite observations, while in the Antarctic (mean for the region 55S-70S) the sign of SIE-TCF correlation depends on season (Mokhov and Chernokulsky, 2014).

We found that SIE-TCF correlation depends on the phase of the Antarctic Oscillation (AAO). In particular, it is negative and significant in the negative phase of AAO (AAO–) ($R_{\text{NSIDC–PATMOS-x}} = –0.64$; $R_{\text{NSIDC–CMSAF}} = –0.5$), while in positive phase (AAO+) the correlation is insignificant (Fig.1) (Mokhov and Chernokulsky, 2016).

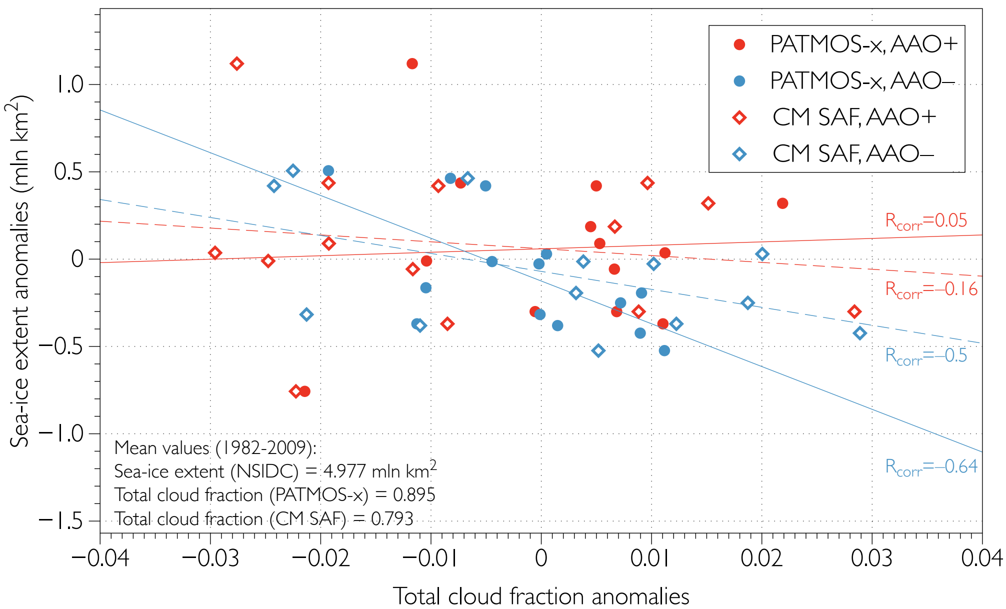

Figure 1. Sea-ice extent (NSIDC) and total cloud fraction (PATMOS-x and CM SAF) anomalies in the Antarctic region (55S-70S) in February-March-April (1982-2009) for AAO positive and negative phases (1982-2009).

The major changes of SIE and TCF, that associated with AAO, are noted in the Weddell, Ross and Bellingshausen Seas, and in the Southern Ocean to the north of

Victoria Land (Figure 2). Difference of sea-ice concentration (SIC) between AAO+ and AAO– reaches 30–40% (up to 50% near Victoria Land). This may be associated with opposite changes of TCF and associated with it cloud-radiative effect (CRE) (changes of radiative fluxes at the top of the atmosphere (TOA) between clear-sky and cloudy conditions) (Figure 2).

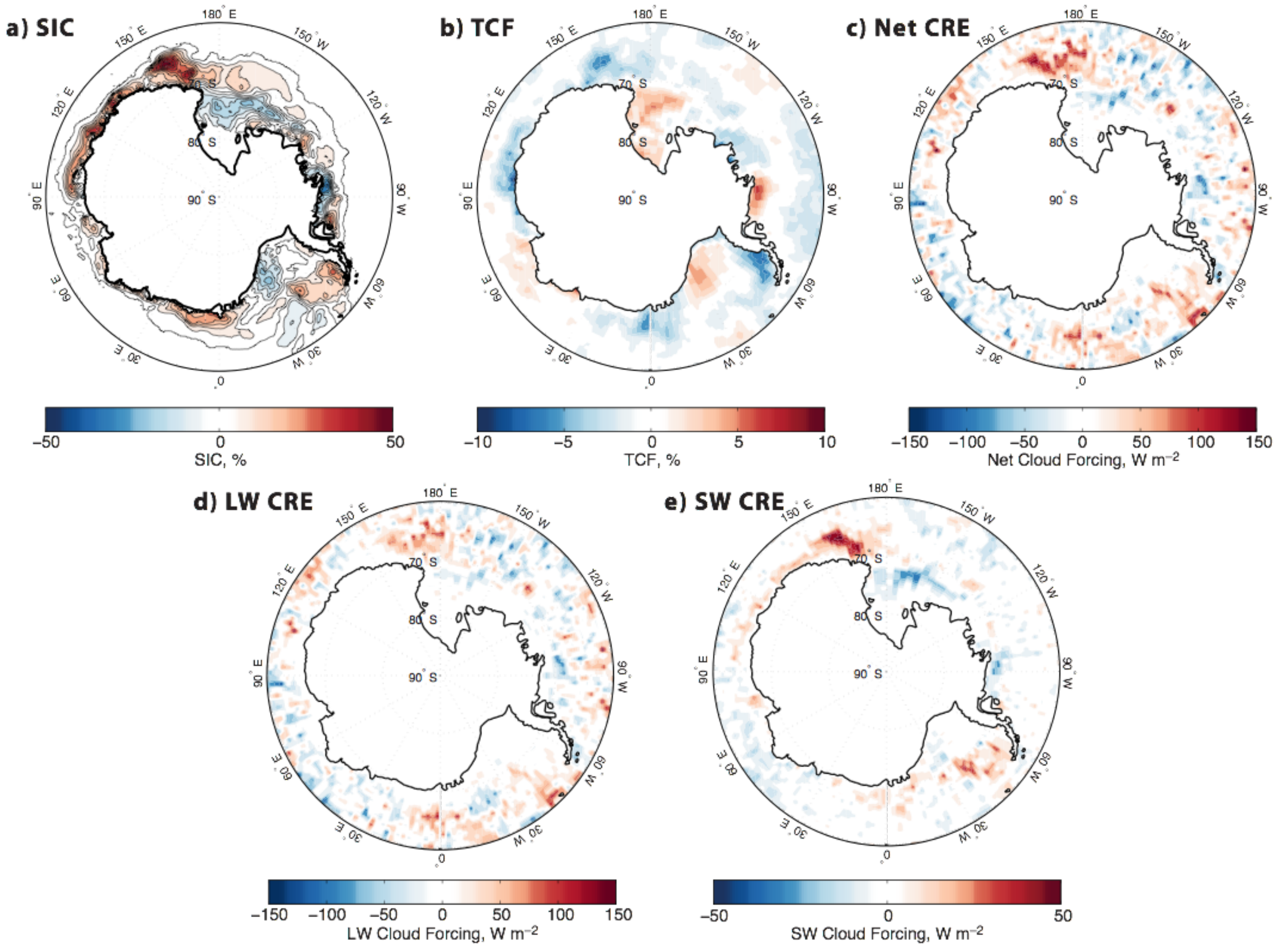

Figure 2. Difference between 4 years of AAO+ (2005, 2009, 2013, 2014) and 4 years of AAO– (2002, 2003, 2004, 2007) in February-March-April of SIC (NSIDC) (a), TCF (CERES) (b), TOA net CRE (CERES) (c), TOA short-wave (SW) CRE (CERES) (d), TOA long-wave (LW) CRE (CERES) (e).

The study have been supported by the RFBR and RAS programs.

References:

Chernokulsky A.V., Esau I., Bulygina O.N., Davy R., Mokhov I.I., Outten S., Semenov V.A. Climatology and interannual variability of cloudiness in the Atlantic Arctic from surface observations since the late 19th century // J. Climate. 2017. V. 30, No. 6, P.2103-2120. DOI: 10.1175/JCLI-D-16-0329.1.

Mokhov I.I., Chernokulsky A.V. Cloudiness and sea ice mutual variations in the Antarctic and Arctic // 2014 SCAR Open Science Conference. Abstracts. 2014. P.198.

Mokhov I.I., Chernokulsky A.V. Sea ice, cloudiness and surface air temperature: Relationships in the Antarctic and Arctic regions from observations and model simulations // 2016 SCAR Open Science Conference. Abstracts. 2016. P.S01.10.

Comparison of temperature in the upper mesosphere from lidar measurements, satellite and model data and from ground-based measurements of hydroxyl emission

M.S. Ivanov[1], I.I. Mokhov[2], A.I. Semenov[2], V.V. Sumarokov[1]

[1] Fedorov Institute of Applied Geophysics, Roshydromet
[2] A.M. Obukhov Institute of Atmospheric Physics RAS
mokhov@ifaran.ru

Temperature at the mesopause level is monitored at the Zvenigorod Scientific Station of the A.M. Obukhov Institute of Atmospheric Physics RAS (ZSS IAP RAS) since the late 1950s (Shefov et al., 2006). This temperature is detected with a diffraction spectrograph from the hydroxyl emission spectra with the maximum emission at an altitude of about 87 km (Semenov et al., 2002; Shefov et al., 2006). Since 2011, the Fedorov Institute of Applied Geophysics has been measuring vertical distributions of temperature and ozone content in the atmosphere with a multifunctional high-altitude sounding lidar. In March 2015, a series of joint lidar (Moscow, 56°N, 37°E) and spectrophotometric (ZSS IAP RAS, 56°N, 37°E) temperature measurements at the mesopause level were conducted. During the lidar soundings, the altitude distributions of the atmosphere temperature were determined up to a height of about 100 km. The temperature profiles from lidar measurements were compared with satellite (AURA, TIMED/SABER), model (CIRA) temperature data.

Figure 1 presents the altitude profiles for temperature from the lidar measurements in comparison with satellite measurements and CIRA model data and with temperature data from spectral measurements of the hydroxyl emission.

The results of the comparison show quite a good agreement for temperature from lidar and hydroxyl emission measurements.

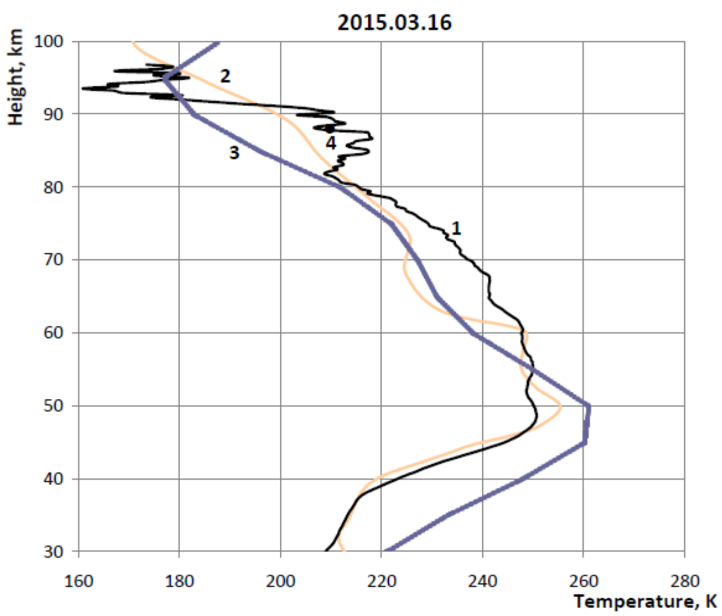

Fig. 1a

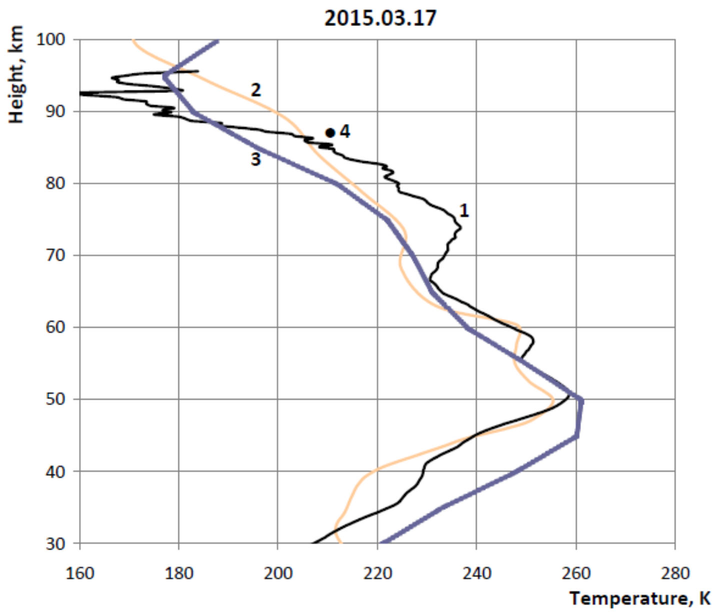

Fig. 1b

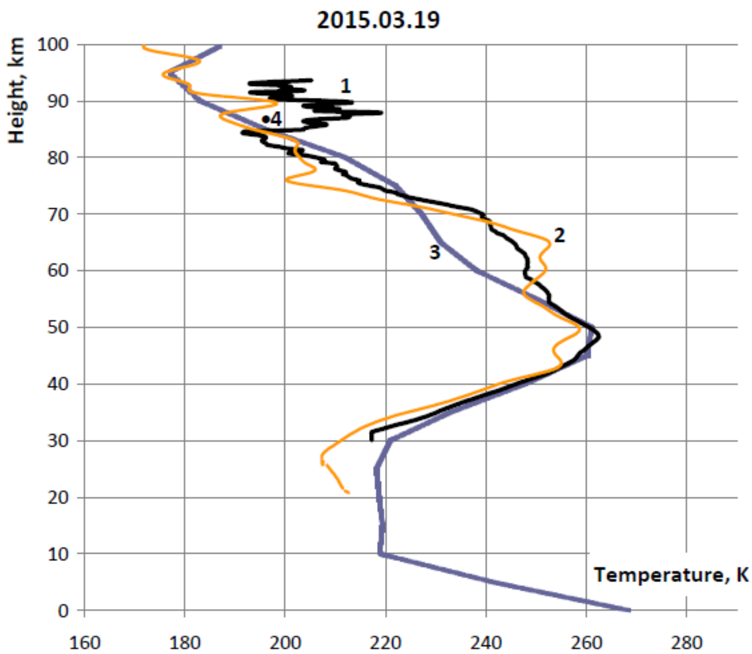

Fig. 1c

Fig. 1. Comparison of temperature profiles for Moscow region from lidar measurements (1) with satellite data (2) and CIRA model (3) and also with temperature at the mesopause from ground-based measurements of hydroxyl emission (4- black circle): a) 16.03.2015, b) 17.03.2015, c) 19.03.2015.

References

Khomich V.Yu., Semenov A.I., and N.N. Shefov (2008) Airglow as an Indicator of Upper Atmospheric Structure and Dynamics. Berlin Heidelberg: Springer-Verlag. 739 p.

Semenov A.I. and N.N. Shefov (1999) Empirical model of hydroxyl emission variations. *Intern. J. Geomagnetism and Aeronomy*, **1**(3), 229-242.

Semenov A.I., V.V. Bakanas, V.I. Perminov, Yu.A. Zheleznov and Yu.V. Khomich (2002) The near infrared spectrum of the emission of the nighttime upper atmosphere of the Earth. *Geomagnetism and Aeronomy*, **42**(3), 390-397.

TROPICAL CYCLONES ACTIVITY IN THE WESTERN NORTH PACIFIC OCEAN: RELATIONSHIP WITH ENSO

Mokhov I.I.[1,2], Timazhev A.V.[1]

[1] *A.M. Obukhov Institute of Atmospheric Physics RAS, Moscow*
[2] *Lomonosov Moscow State University, Moscow*
mokhov@ifaran.ru

Western North Pacific Ocean (WNP) basin is characterized by the largest activity of tropical cyclones (TC). According to (Mokhov et al., 2014) annually about 9 of 25 TCs in the WNP basin from observations since 1970 are transformed into extratropical cyclones. The TC activity in the WNP basin shows strong interannual variations (with standard deviation larger than 4 TC per year) with significant influence of the El Niño / Southern Oscillation (ENSO).

We analyze here relationship with ENSO of the TC activity in the WNP basin using the data from (http://www.meteoinfo.ru/tropicyclones) for TCs and different El Niño indices for the period 1970-2016.

Figure 1 shows integral and local wavelet-spectra for the annual number of WNP TCs (a) and El Niño indices Nino3 (b) and Nino4 (c) in January for the period 1970-2016. Figure 1a exhibits maximum for the period about 4 years and maximum for interdecadal variations. Such maxima are characteristic for the El Niño processes. It is noted remarkably larger contribution of interdecadal variability for Nino4 and for TCs in WNP basin than for Nino3.

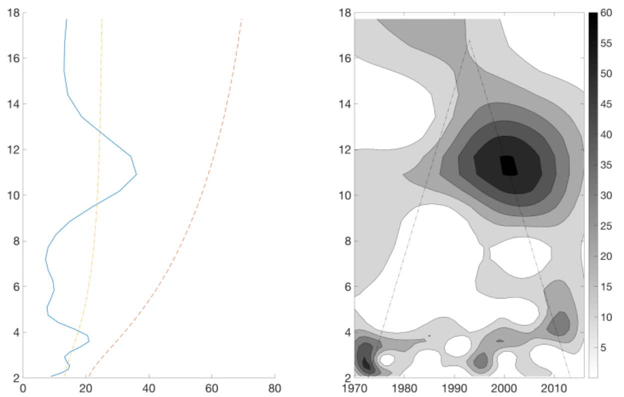

a

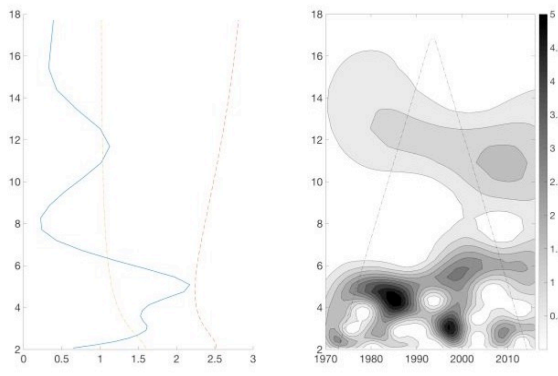

b

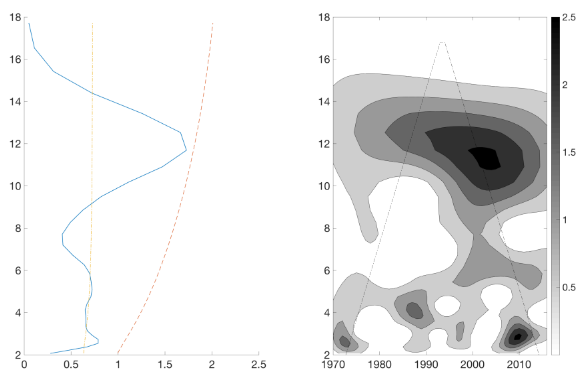

c

Fig. 1. Integral (left) and local (right) wavelet-spectra for the annual TC number for WNP basin (a) and El Niño indices Nino3 (b) and Nino4 (c) in January for the period 1970-2016 (ordinate - periods [years], abscissa – time [years]).

Figure 2 shows local wavelet coherence of the El Niño indices Nino3 (a) and Nino4 (b) in January with the annual number of tropical cyclones for WNP basin for the period 1970-2016. According to Fig. 2 the coherence between El Niño indices and TC number variations with periods about 5 years is more statistically significant since 1990s (with negative correlation).

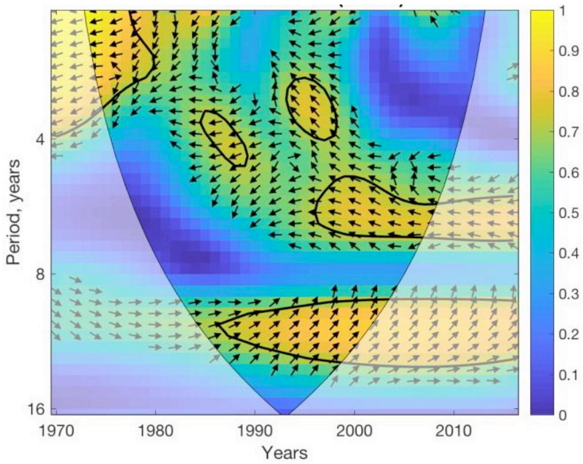

a

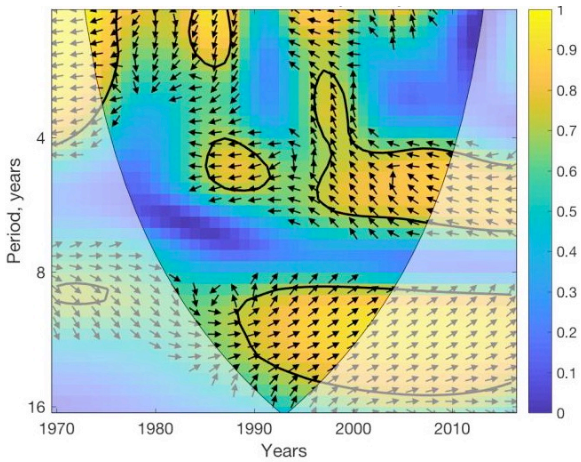

b

Fig. 2. Local wavelet coherence of the El Niño indices Nino3 (a) and Nino4 (b) in January with the annual number of tropical cyclones for WNP basin for the period 1970-2016.

Local coherence between El Niño indices and TC number interdecadal variations is more statistically significant since the end of 1980s (with positive correlation).

This work was supported by the RFBR and RAS.

References

Mokhov I.I., E.M. Dobryshman and M.E. Makarova (2014) Extratropical transition of tropical cyclones: Tendencies of change. *Doklady Earth Sci.,* **454**(1), 59-63.

Behaviour of ensembles in a rotating field
(numerical experiment)

Pokhil A.E.

Hydrometcenter of Russia, 123242, Moscow, Bolshoy Predtechenskiy per. 9-11
e-mail: AEPokhil@yandex.ru

Weather variability is connected with the origination, evolution, interaction of flows and vertical systems in the atmosphere. The huge Antarctic is a real “forge” of vortices systems. When observing, using satellite imagery, the dynamics of chains of cyclones, as if streaming down the Antarctic, one can see that these vortices interact with each other, catching up one another, merging, moving apart, pumping one another energetically, strengthening and weakening one another.

In the present paper the evolution of ensembles of distributed vortices in a rotating field is studied using a numerical model /1/. The rotating field was simulated as a large vortex (a “vortex-field”) with its center being located in the center of the system under investigation.

A few series of experiments were carried out in order to estimate the influence of different parameters of the system under investigation (from one to six vortices) on their behavior. The present short study is a part of the whole investigation.

1st series. The change in the interaction of the “vortex-field” and a “small” eddy with the change of the distance between them is studied.

When placing a “small” eddy into the rotating field, we observe the change of the structure of the eddy itself and of the resulting wind field (Fig.1), since positive and negative velocities of the two vortices sum up. When placing the “small” eddy at different distances from the center of the “field-vortex” (Fig. 1 a,b,c), the velocities and the gradients of velocities in the area of its location are different, and the distortion of the shape of the vortex and the field are different, respectively. This changes the kind of their interaction and the trajectories of their centers motion (Fig. 1, below). In the case “a” the center of the “vortex-field” during the integration remains in the initial position, whereas the “small” eddy rotates around the system center, gradually approaching it. When it approaches it closest, its trajectory describes a loop, and then both the “small” eddy and the “vortex-field” form a structure with a common center. In the experiment “b” at a certain moment the vortex and the eddy form an integrate vortices system, whose center turns out to be somewhat displaced with respect to its initial position. Such trajectories were observed in our previous studies /2/. During a certain time period the “small” eddy moves following a cyclonic orbit towards the edge of the field, forming a series of “secondary” vortices in its rear.

2nd series. The interaction of two, three and four vortices in a rotating field is studied (Fig. 1 d,e,f). In the experiment “d”, where the location of two “small” eddies, at a certain distance from one another, is symmetrical with respect to the field center, we observe steady balance in the interaction of vortices (practically at the same, constant, distance) with cyclonic rotation. In the experiment “e”, “f” (Fig. 1 e,f) secondary “small” eddies form /3/. As a result of this the centers of the initial eddies move apart (are “pushed one away from the other”). In the case “e” at the beginning of the experiment the system tries to bring the eddies to equilibrium (locating the centers of the eddies in the form of an isosceles triangle), but, further on, the system dynamics breaks down, and we see that they move apart (are “pushed away from each other”) with different speeds.

So, introducing a rotating field leads not only to the displacement of the system of small eddies to a certain distance at a certain speed (which depends on the relationship between the characteristics of the central vortex and small eddies and on their number), but it displaces different parts of small eddies with different speeds deforming them. Owing to the deformation small eddies begin: a) to interact with each other more intensely or weaker, b) in certain conditions secondary eddies form behind them, which also makes their contribution to the motion and the interaction of small eddies.

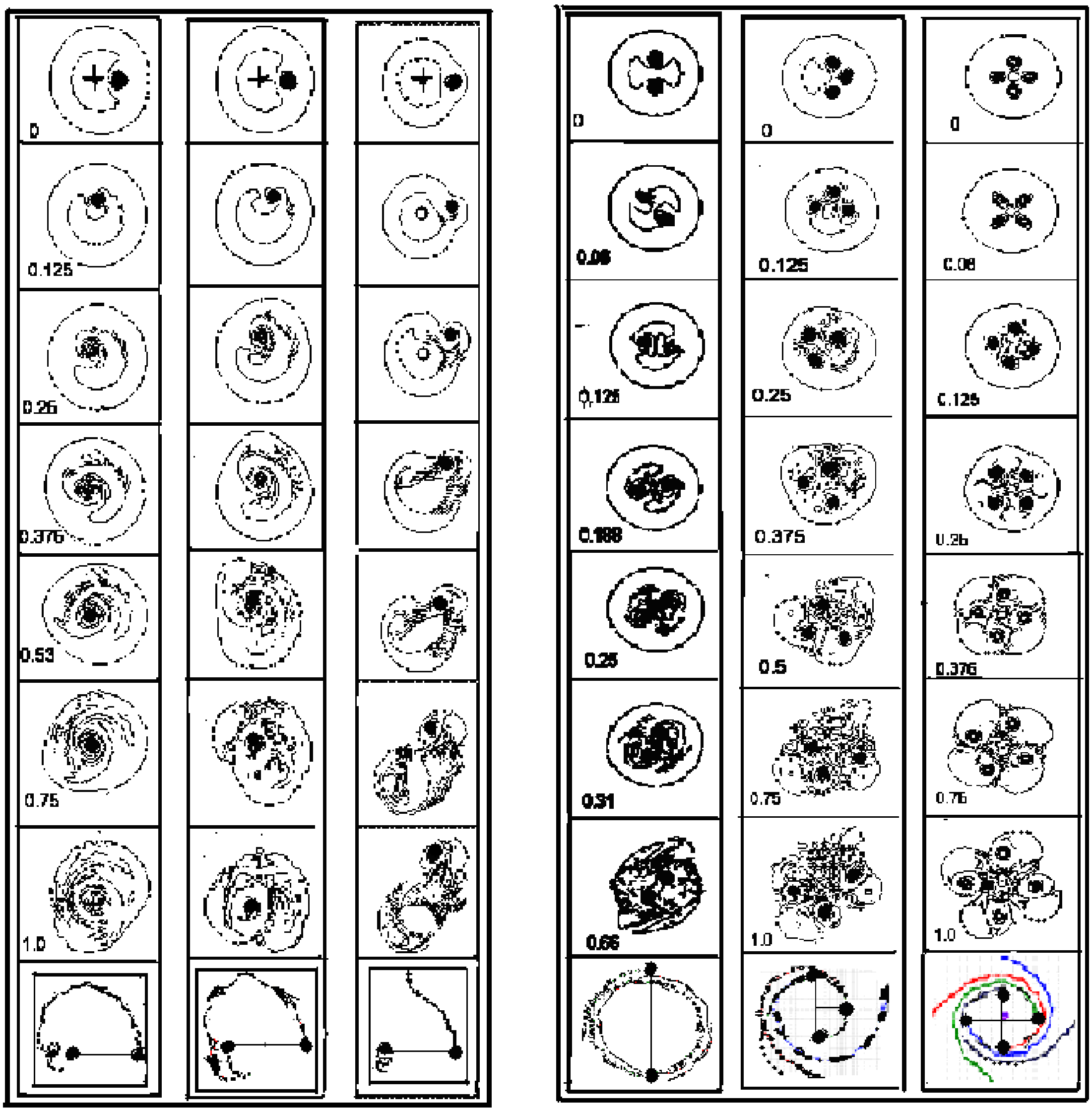

a b c d e f

Fig. 1 a – f. Dynamics of the vortices of a group of eddies and the trajectories of the motion of their centers (in the lower part of the figure). The calculations are made using model [1]. Figures indicate the relative time of integration.
a, b, c – a small eddy placed at different distances from the system center.
d, e, f – experiments with two, three and four eddies.

References

1. Sitnikov I.G., Zlenko V.A. Experience of numerical forecast of the tracks of tropical cyclones. – Meteorology and Hydrology, 1987, No. 8, pp. 40 – 47.
2. Pokhil A.E. Study of the cases of formation of “small” eddies in the atmosphere. //Proceedings of Hydrometcentre of Russia. – 2016. –Vol. 362- p.172-192.
3. Margolin A., Pokhil A. About the formation of a cloud of small vortices in the case of the interaction of a few larger vortices of finite dimensions. Res.Act.Atm. Ocean Model.-2000. – WMO/TD - N39 - P.25-26.

Frontogenesis in a tropospheric frontal zone: a case study

N. P. Shakina, N. I. Komas'ko, A. R. Ivanova
Hydrometeorological Research Center of Russia, Moscow, Russia

Frontogenesis defined as a process of temperature horizontal gradient change in the air particle represents one of main mechanisms for properties redistribution between different scales of motion. Frontogenesis plays an important role in forcing vertical circulations. In the ascending branches of the circulation cells, at the atmospheric surface fronts, clouds and precipitation develop. In the upper and middle troposphere and in the jet stream layers, the descending branches generate stratospheric intrusions – areas of stratospheric and sub-stratospheric air sinking to the tropospheric levels.

In the paper, a case of upper-level frontogenesis over Russia is analyzed on the real (objective analysis) data. For this purpose, two components – Q_n and Q_s - of the vector frontogenetical function $\boldsymbol{Q}$ are calculated, the s and n axes being directed along and across the isentrope (the potential temperature, θ, contour):

$$Q_n = \frac{1}{2}|\nabla\theta|[D - E_{sh}\sin 2\alpha - E_{st}\cos 2\alpha],$$
$$Q_s = \frac{1}{2}|\nabla\theta|[\zeta - E_{st}\sin 2\alpha + E_{sh}\cos 2\alpha] \quad (1)$$

In (1), D is the velocity divergence at the H level, E_{st} and E_{sh} are the stretch and shear deformations, respectively, ζ is the relative vorticity, α is the angle between the x axis (directed eastward) and $\nabla\theta$.

Q_n is frontogenetical component or scalar frontogenesis function, and Q_s is rotational component (Keyser *et a*l., 1988). Also, the right-hand side of the ω-equation

$$N^2\nabla_p^2\omega + f^2\frac{\partial^2\omega}{\partial p^2} = -2\nabla_p\cdot\vec{Q}. \quad (2)$$

is considered. In (2), N is the Brunt-Vaisala frequency, $\omega = dp/dt$ is the vertical velocity, p is the pressure, f is the Coriolis parameter, the ∇_p operator is related to the isobaric surface.

The calculations are carried out on the objective analysis data with horizontal resolution of 1.25° both in latitude and longitude for the period of December 11 to 15, 2013, when over European Russia a warm front was situated associated with a deep low centered in Scandinavia. The tropospheric frontal zone over and ahead the front surrounded a deep, narrow trough whose axis was oriented from NE to SW. The situation has much in common with the conceptual model by Shapiro (1081) at the stage when a closed low develops in a deep trough. At the NE branch of the frontal zone, a strong jet stream exists with a jet streak, at the entrance of which, a deep stratospheric intrusion (streamer) develops at its cold side.

The calculated rotational component, Q_s, is found to force a band of intense descending motions inside the streamer (Fig.1). Along its axis, a chain of deep minima of tropopause height (maxima of pressure at the 4 *pvu* surface) are obtained. Physical consistence of these minima is questionable because of restricted horizontal resolution of the data under use. On the other hand, the findings by Appenzeller *et al* (1996) have proven that the real stratospheric intrusions are subject to fragmentation into chains of smaller funnels and eddies, similar to some extent to those shown in Fig. 1, b.

The frontogenetical component, Q_n, at the cold side of the fontal zone and jet stream gives rise to strong descending motions and contributes the stratospheric intrusion deepening, while at the warm side, it forces intense ascending in the 500-250 hPa layer, as a result of isotherm turning in the south part of the tropospheric trough (Fig. 2).

Thus, both scalar and rotational components of the vector frontogenetical function force, in the situation under consideration, thermally direct circulations. The maxima of both components are of the same order of magnitude, but they act in different parts of the field. In accordance with the Shapiro conceptual model, at the approximately linear part of the frontal zone, the scalar frontogenesis plays the primary role in the stratospheric intrusion development, while in the zone of the streamlines maximum curvature, such role is played by the rotational frontogenesis.

References

Appenzeller C., H.C. Davies, W. A. Norton, 1996: Fragmentation of stratospheric intrusion. J. Geoph. Res., v. 101, D, 1435-1456/

Keyser D., M. J. Reeder, R. J. Reed, 1988: A generalization of Petterssen’s frontogenesis function and its relation to the forcing of vertical motion. Mon. Wea. Rev., v. 116, pp. 762-780.

Shapiro M. A., 1981: Frontogenesis and geostrophically forced secondary circulation in the vicinity of jet-stream-frontal zone systems. J. Atmos. Sci., v. 38, pp. 954-973.

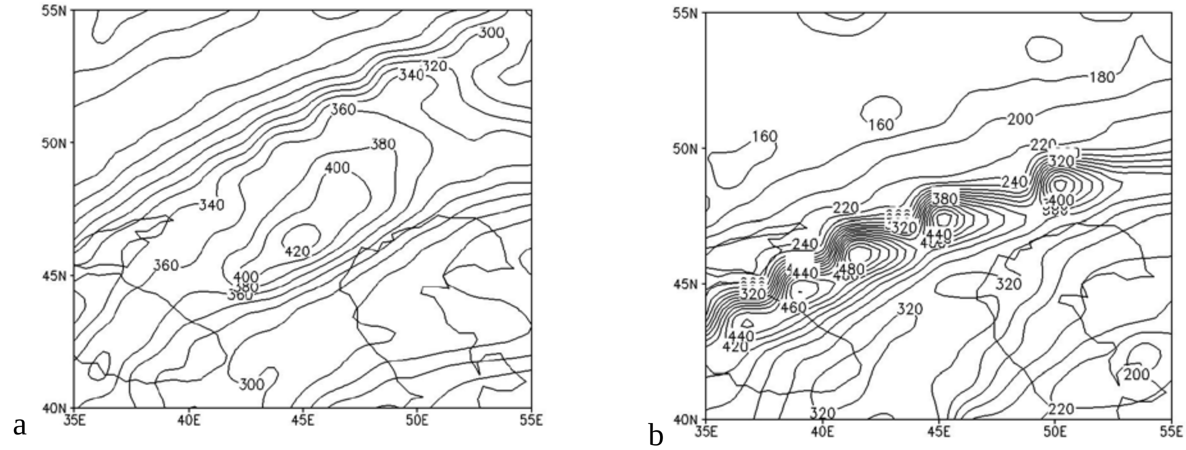

Fig. 1. Tropopause height (pressure, hPa, at the 4 *pvu* surface) at 00 (a) and 12 (b) UTC, December 12, 2013.

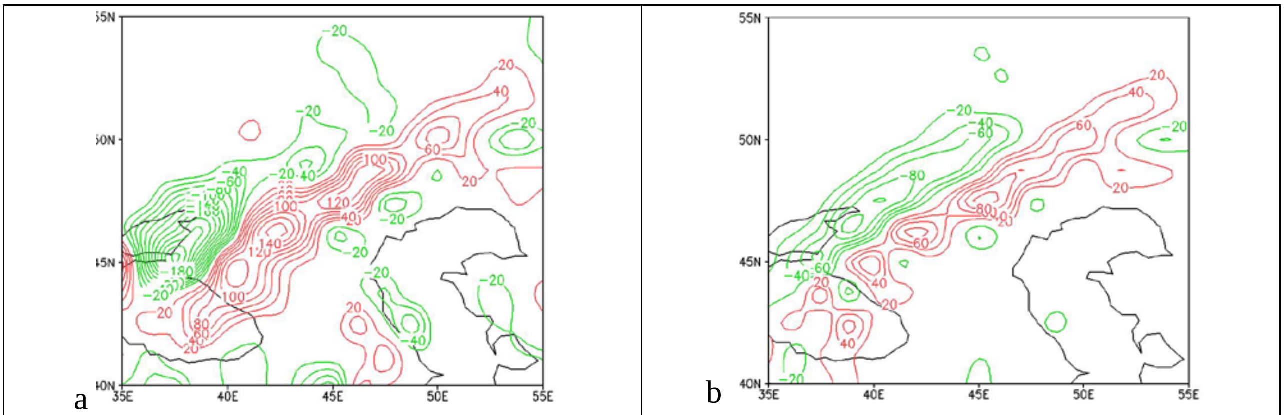

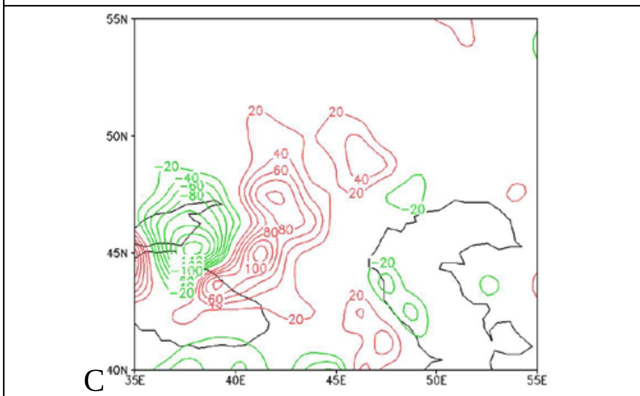

Fig. 2. Divergence contours of $\boldsymbol{Q}$ (a), Q_n (b), and Q_s (c), 10^{-16} K $(s.m^2)^{-1}$, at the 500 hPa level, 12 UTC, December 12, 2013: contours corresponding to ascending and descending motions are green and red, respectively.

Can Arctic sea ice loss drive teleconnection patterns into the midlatitudes?

Ian Simmonds and Irina Rudeva

School of Earth Sciences, The University of Melbourne, Victoria 3010, Australia simmonds@unimelb.edu.au

The dramatic decrease of Arctic sea ice extent in recent times (Simmonds 2015) has prompted questions as to what the *direct* of effect this might be on midlatitude weather and climate. At present there are a number of disparate views on this (Screen et al. 2013; Simmonds and Govekar 2014; Luo et al. 2016a, b; Chen et al. 2016; Luo et al. 2017a, b; Yao et al. 2017; Blackport and Kushner 2017)).

We are using simple ray tracing techniques to explore the possibility of robust Rossby wave trains being forced from within the Arctic. The key to this is not surface temperature (Ts) or fluxes *per se* but rather whether there is a link between Ts and precipitation (and hence convective heating). We have correlated the detrended seasonal means of ERA-Interim Ts and Global Precipitation Climatology Project (GPCP) precipitation. Fig. 1 shows that these correlations are, at best, modest particularly in summer. They cast into doubt the possibility of the Arctic region driving robust teleconnections into the midlatitudes.

References

Blackport, R., and P. J. Kushner, 2017: Isolating the atmospheric circulation response to Arctic sea ice loss in the coupled climate system. *J. Climate*, **30**, 2163-2185.

Chen, H. W., et al., 2016: The robustness of midlatitude weather pattern changes due to Arctic sea ice loss. *J. Climate*, **29**, 7831-7849.

Luo, B., et al., 2017: Atmospheric circulation patterns which promote winter Arctic sea ice decline. *Env. Res. Lett.*, **12**, 054017.

Luo, D., et al., 2017: Increased quasi-stationarity and persistence of winter Ural Blocking and Eurasian extreme cold events in response to Arctic warming. Part II: A theoretical explanation. *J. Climate*, **30**, 3569–3587.

Luo, D., et al., 2016: Impact of Ural Blocking on Winter Warm Arctic–Cold Eurasian Anomalies. Part II: The Link to the North Atlantic Oscillation. *J. Climate,* **29**, 3949-3971.

Luo, D., et al., 2016: Impact of Ural Blocking on Winter Warm Arctic–Cold Eurasian Anomalies. Part I: Blocking-Induced Amplification. *J. Climate*, **29**, 3925-3947.

Screen, J. A., et al., 2013: The atmospheric response to three decades of observed Arctic sea ice loss. *J. Climate*, **26**, 1230-1248.

Simmonds, I., 2015: Comparing and contrasting the behaviour of Arctic and Antarctic sea ice over the 35-year period 1979-2013. *Ann. Glaciol.*, **56(69)**, 18-28.

Simmonds, I., and P. D. Govekar, 2014: What are the physical links between Arctic sea ice loss and Eurasian winter climate? *Env. Res. Lett.*, **9**, 101003.

Yao, Y., et al., 2017: Increased quasi-stationarity and persistence of winter Ural Blocking and Eurasian extreme cold events in response to Arctic warming. Part I: Insights from observational analyses. *J. Climate*, **30**, 3549–3568.

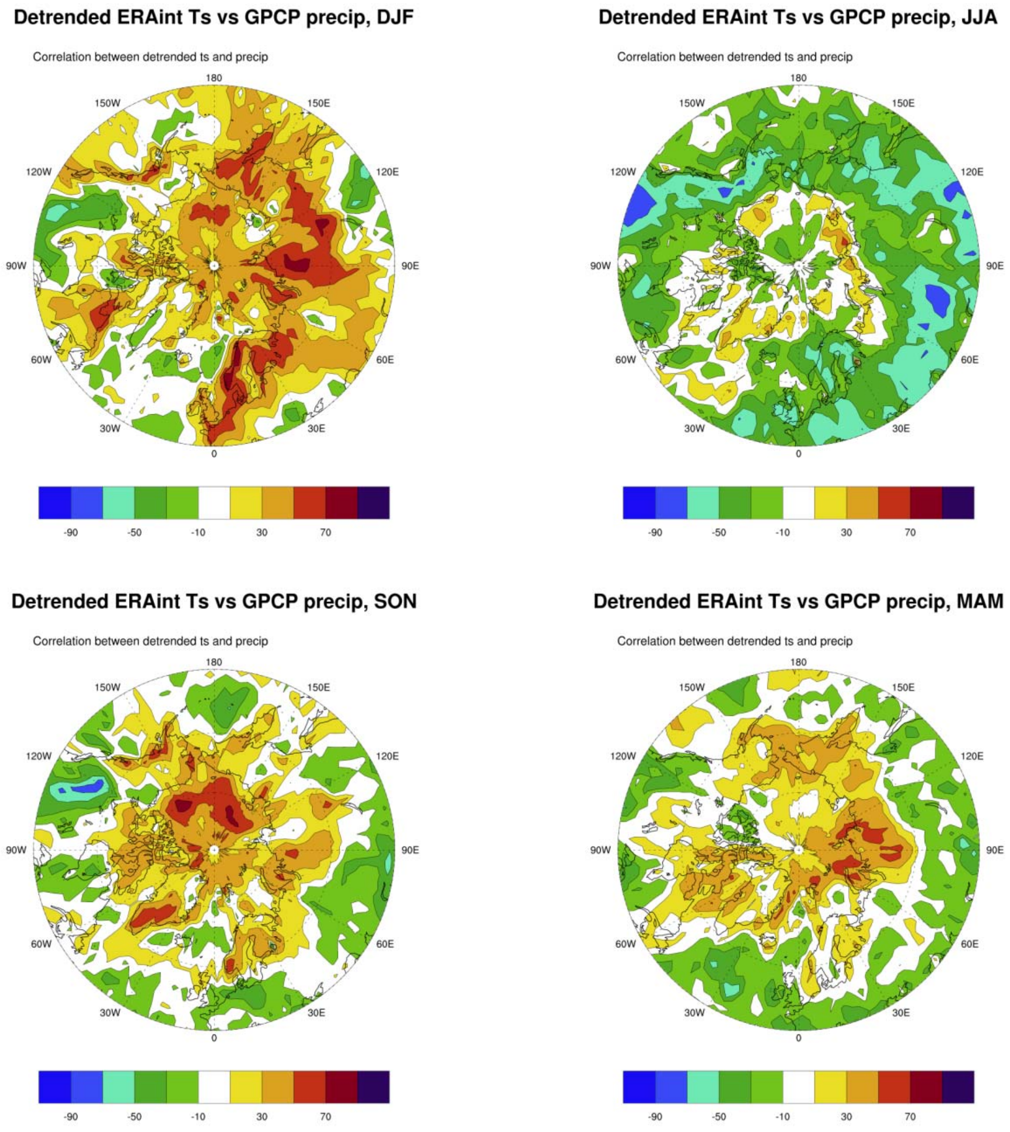

Fig . 1: Correlations of detrended seasonal means of ERA-Interim *T*s and GPCP precipitation

Strong links between the Southern Hemisphere subtropical ridge and frontal behaviour

Ian Simmonds, Irina Rudeva and David Crock

School of Earth Sciences, The University of Melbourne, Victoria 3010, Australia
simmonds@unimelb.edu.au

Considerable research activity is presently being directed at diagnosing trends in the Hadley circulations and also the behaviour of frontal systems. These two can be seen to be connection through the requirement of 'seamless' meridional energy fluxes across the tropics and the midlatitudes.

We are exploring these relationships in the Southern Hemisphere making use of the ERA-Interim reanalysis and The University of Melbourne frontal analysis scheme (Catto et al., 2015; Hope et al., 2014: Papritz et al., 2014: Rudeva and Simmonds, 2015: Schemm et al., 2015: Simmonds et al., 2012). Figure 1 shows very strong interannual relations between the latitude of the subtropical ridge (STR, an index of the extent of the Hadley cell) and the frequency of strong fronts in the 20-40^{o}S latitude belt. The plots and the associated correlation coefficients point to a very strong interannual relations between these variables.

References

Catto, J. L., et al., 2015: Global relationship between fronts and warm conveyor belts and the impact on extreme precipitation. *J. Climate*, **28**, 8411-8429.

Hope, P., et al., 2014: A comparison of automated methods of front recognition for climate studies: A case study in southwest Western Australia. *Mon. Wea. Rev.*, **142**, 343-363.

Papritz, L., et al., 2014: The role of extratropical cyclones and fronts for Southern Ocean freshwater fluxes. *J. Climate*, **27**, 6205-6224.

Rudeva, I., and I. Simmonds, 2015: Variability and trends of global atmospheric frontal activity and links with large-scale modes of variability. *J. Climate*, **28**, 3311-3330.

Schemm, S., et al., 2015: Extratropical fronts in the lower troposphere: Global perspectives obtained from two automated methods. *Quart. J. Roy. Meteor. Soc.*, **141**, 1686-1698.

Simmonds, I., et al., 2012: Identification and climatology of Southern Hemisphere mobile fronts in a modern reanalysis. *J. Climate*, **25**, 1945-1962.

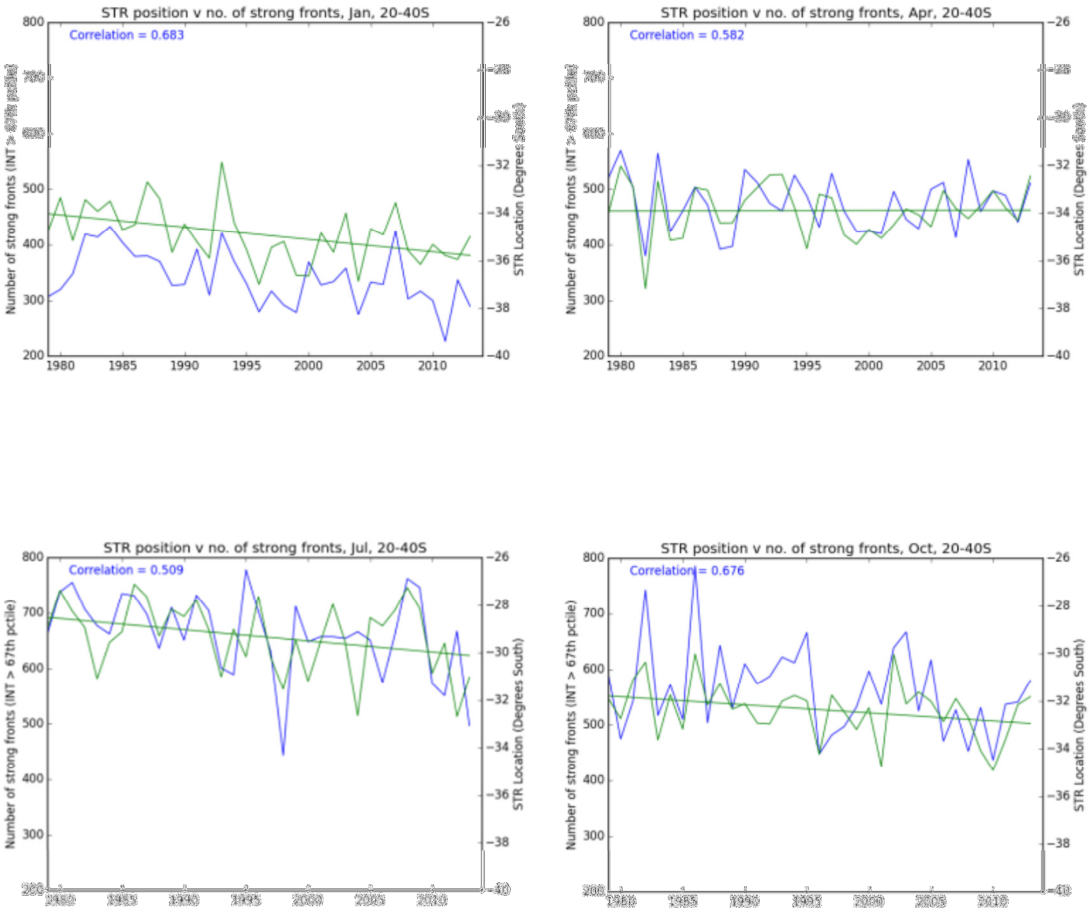

Fig . 1: Time series of the latitude of the Southern Hemisphere STR (green line) and the number of strong fronts lying within 20-40^{o}S (blue line) for January, April, July and October. The (significant) correlations between the time series are 0.68, 0.58, 0.51 and 0.68 for these months, respectively.

The effect of different criteria on tracking eddy in the South China Sea

Meng Zhang[1], Hans von Storch[1], Delei Li[2]

1. Institute for Coastal Research, Helmholtz Zentrum Geesthacht, Geesthacht, Germany
2. Institute of Oceanology, Chinese Academy of Sciences, Qingdao, China

meng.zhang@hzg.de

Ocean eddies with great energy play a vital role on the mixing and transport of ocean water, heat and mass (Faghmous et al., 2015). A 1/10-degree daily global ocean simulation STORM (from the German consortium project STORM) forced by the NCEP reanalysis-1 provides the access to resolving the variability of the global eddy (von Storch et al., 2012). In this paper, we discuss the effect of different criteria on identifying and tracking eddy in the South China Sea (SCS). There are mainly three steps in the process of tracking eddy: eddy detecting, eddy tracks connecting and tracks filtering. In the tracking process, small difference in criteria selecting can lead to quite different results. In this paper, we evaluated the effect of different criteria based on a series of sensitivity tests of the year 2001.

We define the extrema of sea surface height anomaly (SSHA), which is greater or less than its 24 neighbors as eddy (Faghmous et al., 2015). Eddy intensity is defined as the difference between the extremum and averaged SSHA of its 24 neighbors. Only eddy intensity stronger than certain threshold (threshold_A) will be chosen. Considering eddy travel speed and the spatial resolution of STORM, we define another value (threshold_B) as the limitation of eddy travelling distance within one day. When filtering tracks, the strongest eddy intensity within a track should fulfill certain thresholds (threshold_C). Furthermore, the selected tracks must travel over 100km, and the distance between the final position and the initial position should be over 50km. The tracked results (like Figure 1) will be used to analyze the variability of the eddy in the SCS.

In our sensitivity tests, threshold_A varies from 1mm to 7mm (Min_I_1mm … Min_I_7mm). Threshold_B is set as 20km or 25km (dis_20, dis_25). And threshold_C increases from 2mm to 10mm (Strongest_2mm … Strongest_10mm). The tables show the eddy track numbers (top) and the mean eddy travel lengths (bottom) in the various combinations.

Almost always, more cyclonic than anti-cyclonic eddy tracks are detected. Not surprisingly, the number of eddies decreases, when the minimum eddy intensity and the minima of the strongest intensity along the track are increased. The track lengths increase for almost all cases, when the minimum eddy intensity is lowered and when the minimum maximum intensity along the track is increased. An exception emerges, when the minimum maximum intensity is up to 10mm; then the number of anti-cyclonic eddies tracks is getting very small. If a distance for connecting daily eddies is increased from 20km to 25km, more tracks are detected. We conclude that results depend sensitively on the threshold of minimum maximum eddy intensity along the track and on the minimum eddy intensity.

Figure: The anti-cyclonic eddy tracks (left) and the cyclonic eddy tracks (right) for a given set of parameters: Min_I_3mm, dis_20 and Strongest_4mm.

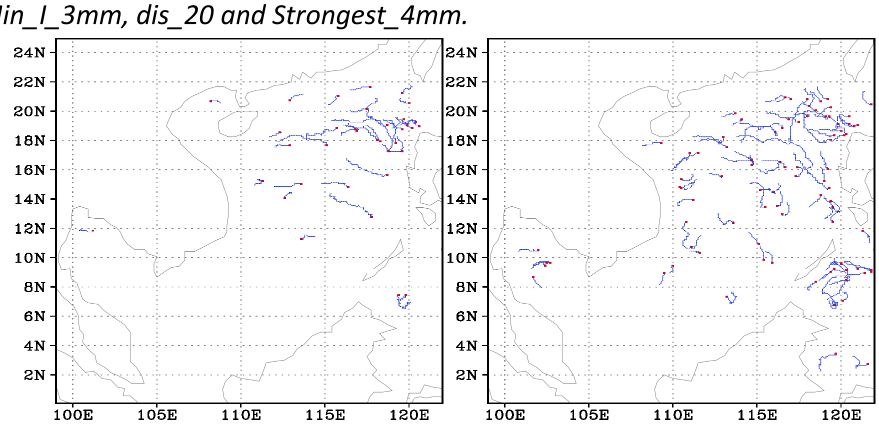

Table: The number of eddy tracks (top) and mean travel length of the eddy (bottom) when different parameters are set. "Anti" and "Cyc" mean anti-cyclonic eddy and cyclonic eddy respectively.

Number of_tracks		Min_I_1mm		Min_I_3mm		Min_I_5mm		Min_I_7mm	
		Anti	Cyc	Anti	Cyc	Anti	Cyc	Anti	Cyc
Strongest_2mm	dis_20	64	122	-	-	-	-	-	-
	dis_25	125	185	-	-	-	-	-	-
Strongest_4mm	dis_20	43	103	36	87	-	-	-	-
	dis_25	86	151	72	128	-	-	-	-
Strongest_6mm	dis_20	22	76	19	73	13	52	-	-
	dis_25	48	114	46	108	35	85	-	-
Strongest_8mm	dis_20	14	54	14	53	11	44	7	26
	dis_25	35	85	34	82	31	72	19	47
Strongest_10mm	dis_20	7	31	7	31	6	29	4	22
	dis_25	21	56	20	55	19	53	13	43

Mean_Length (km)		Min_I_1mm		Min_I_3mm		Min_I_5mm		Min_I_7mm	
		Anti	Cyc	Anti	Cyc	Anti	Cyc	Anti	Cyc
Strongest_2mm	dis_20	217	198	-	-	-	-	-	-
	dis_25	240	237	-	-	-	-	-	-
Strongest_4mm	dis_20	238	204	210	198	-	-	-	-
	dis_25	252	251	206	221	-	-	-	-
Strongest_6mm	dis_20	252	217	211	208	211	179	-	-
	dis_25	253	263	212	230	184	204	-	-
Strongest_8mm	dis_20	271	222	237	216	230	184	208	201
	dis_25	257	267	222	240	192	210	168	200
Strongest_10mm	dis_20	170	255	170	243	177	196	197	217
	dis_25	213	271	187	236	167	209	155	208

References

Faghmous, J. H., Frenger, I., Yao, Y., Warmka, R., Lindell, A., Kumar, V., 2015. A daily global mesoscale ocean eddy dataset from satellite altimetry. Scientific data, 2.

von Storch, J.-S., Eden, C., Fast, I., Haak, H., Hernández-Deckers, D., Maier-Reimer, E., Marotzke, J., Stammer, D., 2012. An estimate of the Lorenz energy cycle for the world ocean based on the STORM/NCEP simulation. J. Phys. Oceanogr. 42 (12), 2185—2205, http://dx.doi.org/10.1175/JPO-D-12-079.1.